nature communications

Article | Article in Press

https://doi.org/10.1038/s41467-026-79278-y

Engineering phosphorescence and pH-responsive fluorescence of molecular luminophores and elastomers

Received: 29 June 2026

Accepted: 16 October 2026

Published online: 05 November 2026

Check for updates

Dingbowen Wang (王丁博文)[1,2], Jiayue Feng (冯嘉悦)[1,2] & Jian Yang (杨健)[1,2]

Organic ultralong room-temperature phosphorescence (RTP) enables time-gated optical readout by separating long-lived triplet emission from short-lived autofluorescence. However, coupling RTP with biochemical responsiveness at both the molecular and materials levels remains a fundamental challenge due to the lack of a luminophore-intrinsic design principle for linking chemical responsiveness to triplet-state photophysics and the conflict between rigid, shielded microenvironments and deformable polymer matrices. Here we present an ArKMK design paradigm that electronically couples an aromatic ketone to a pH-responsive α-methyleneketone within a carbonyl-rich framework, yielding homophthalic anhydride (HA) and homophthalimides as a family of luminophores that integrate pH responsiveness with RTP. To preserve long-lived emission in elastomeric matrices, we further develop a two-pots-in-one (TPiO) strategy that separately preforms hydrophilic and hydrophobic segments and then co-reacts them to generate phase-separated microenvironments in biodegradable polyesters. The resulting materials reconcile mechanical compliance with triplet-state stabilization, while covalently integrating ArKMK luminophores through the same esterification chemistry. These biodegradable polyesters enable time-gated subcutaneous imaging, gastrointestinal tracking and wound-status reporting through coupled RTP and pH-indicating fluorescence. This work establishes a molecular-to-polymer framework for integrating pH responsiveness with long-lived triplet emission in soft, biodegradable materials.

Organic ultralong room-temperature phosphorescence (RTP), typically a solid-state emission characterized by millisecond-to-second triplet lifetimes[1,2], has attracted broad interest in bioimaging, sensing, anti-counterfeiting, and information encryption due to its ultralong lifetime and sensitive triplet nature compared to the conventional fluorescence. In biological settings, this delayed emission is particularly valuable because time-gated detection can reject short-lived autofluorescence and markedly improve imaging contrast[3,4]. Yet contrast alone is not the end goal for many biomedical applications, where the key unmet need is to report local biochemical states that govern tissue pathophysiological processes[5–9]. Among these cues, pH is particularly informative and broadly relevant[10–13]. Conventional fluorescent pH probes can report such biochemical changes, but provide only prompt, intensity-based optical signals, whereas conventional RTP materials offer temporally separated, persistent emission but are generally passive toward local biochemical states. Integrating these complementary functions within a single material platform therefore enables two distinct optical dimensions: prompt fluorescence for reporting local pH and delayed phosphorescence for persistent, time-

[1]Department of Materials Science and Engineering, School of Engineering, Westlake University, Hangzhou, Zhejiang 310030, China. [2]Research Center for Industries of the Future, Westlake University, Hangzhou, Zhejiang 310030, China. e-mail: yangjian07@westlake.edu.cn

gated readout. Rather than simply combining two optical properties, this integration transforms a passive phosphorescent material into a self-reporting platform that couples biochemical-state reporting with temporally resolved optical information. Over the past decade, substantial effort has been devoted to pushing the limits of brightness and lifetime in RTP materials[14–18], whereas comparatively little attention has been paid to encoding pH responsiveness into molecular design. This gap calls for a molecularly defined strategy in which pH responsiveness and triplet-state photophysics are intrinsically integrated within the same luminophore framework, providing a chemical basis for responsive phosphorescent materials in complex physiological environments.

Most reported approaches to introducing pH responsiveness into RTP systems rely on collective intermolecular interactions or environmental perturbations, making their optical responses strongly dependent on aggregation state, material morphology, and hydration rather than a defined molecular event, which compromises switch-like precision and transferability. We therefore sought to encode pH responsiveness into the luminophore itself while retaining carbonyl-rich motifs that promote intersystem crossing (ISC) and triplet-state stabilization through enhanced $n\rightarrow\pi^*$ character. Building on our previous finding that the α-methyleneketone motif endows homophthalic anhydride (HA) with pH responsiveness[19], we designed an ArKMK (aryl-linked ketone and α-methyleneketone) motif (Fig. 1a), defined as an aryl-linked ketone electronically coupled to an α-methyleneketone. In this motif, the aromatic ketone favors $n\rightarrow\pi^*$ transitions and ISC, whereas the α-methyleneketone undergoes proton-dependent keto-enolate chemistry that renders the electronic structure of the same luminophore sensitive to pH. These two elements are not additive substituents, but electronically integrated components of a carbonyl-rich scaffold. Using HA and its derived imides (homophthalimides) as model systems, we show that this design produces pH-responsive luminophores with excitation-dependent delayed emission arising from isolated-molecule and collective emissive states.

To preserve these molecularly encoded optical functions in soft, deformable and biologically relevant materials, a polymer architecture is needed that can reconcile triplet-state stabilization with mechanical compliance. Elastomers are natural candidates for soft-tissue interfaces, but incorporating RTP into elastomers introduces a fundamental soft-hard contradiction: long-lived phosphorescence favors rigid, protective microenvironments that suppress nonradiative decay and limit oxygen and moisture quenching, whereas elastomeric substrates are designed to be soft, mobile, and permeable. Multiphase engineering offers an elegant solution by combining a compliant continuous phase with locally rigid domains that provide confinement and barrier functions[20]. In practice, controllable phase separation with RTP has thus far been achieved in methacrylate-based block copolymers and polyurethanes[20,21]. Biodegradable polyesters are particularly attractive for tissue engineering[22–24] because their hydrolytic chemistry and degradation profiles can be systematically tuned, their building blocks and degradation products can often be clearly defined, and they may offer favorable biosafety profiles compared with the aforementioned methacrylate-based block copolymers and polyurethanes, without the associated risks of residual cytotoxic monomers, catalysts, or initiators[25–27]. However, robust, programmable molecular strategies that enable the construction and precise modulation of segmented chain architectures to achieve controllable phase separation in polyester elastomers remain exceedingly limited. To this end, we develop a "two-pots-in-one" (TPiO) strategy to control phase-separated microenvironments in polyester elastomers, in which hydrophilic and hydrophobic segments are partially preformed in separate pots and subsequently co-reacted to produce segmented network architectures with controllable meso- to microscale phase separation. The ArKMK luminophores are covalently integrated during network formation via the same esterification chemistry, enabling the design of molecular photophysics and material microenvironments in tandem. With these materials, we demonstrate the biomedical relevance of this platform through three representative demonstrations in mice, including time-gated subcutaneous imaging, gastrointestinal tracking, and a self-reporting wound dressing that couples RTP with pH-indicating fluorescence for wound status indication.

Results

ArKMK integrates pH responsiveness with RTP in luminophores

We have previously demonstrated that homophthalic anhydride (HA) exhibits pH responsiveness due to its α-methyleneketone structure[19]. This suggests that an α-aryl ketone can be adopted to construct pH-responsive luminophores. Aromatic ketones are favorable for RTP because the carbonyl groups promote $n\rightarrow\pi^*$ transitions and facilitate the spin-forbidden singlet-to-triplet transfer through ISC to populate triplet excitons. Notably, the α-methyleneketone motif not only imparts pH responsiveness but also contributes an additional carbonyl, making it a particularly advantageous complement to the aryl ketone for constructing carbonyl-rich RTP scaffolds. Together, we define this synergistic pairing as the "ArKMK" (aryl-linked ketone and α-methyleneketone) design paradigm for building RTP luminophores with robust pH responsiveness (Fig. 1a). Following this design paradigm, we synthesized a series of HA-derived homophthalimides via a facile one-pot condensation of HA with primary amines (Fig. 1a, b), with the notable exception of thioacetamide, which affords 3-Methyl-1(2*H*)-isoquinolinone (HA-TAA) and thus provides a convenient entry to isoquinolinone cores (Fig. S1a).

Several of these compounds, including HA-Gly (HA reacted with glycine), HA-Anl (HA reacted with aniline) and HA-TAA, have been reported previously in synthetic chemistry studies using different synthetic routes or reaction conditions[28–30]. However, their photophysical properties and single-crystal structures have not been previously investigated. The pH responsiveness of the synthesized homophthalimides was examined. Taking HA-Gly as an example: upon adding a base, an aqueous solution changes from colorless to yellow and emits bright green fluorescence under UV irradiation (Fig. 1c, d). As with HA, the response originates from keto-enolate tautomerization at the α-methyleneketone site. As pH increases from 3.8 to 11.7, the fluorescence intensity rises and plateaus near pH 11.3 (Fig. 1e). Fitting the curve yields a pK_a of 9.65 for the α-methyleneketone proton of HA-Gly (Fig. S1b). Notably, the intensity increases by ~3-, 5.5-, and 16-fold when the pH is raised from 6.5 to 7.0, 7.4, and 8.0, respectively (Fig. S1c), underscoring its potential for pH-sensitive biomedical applications. We further tracked the fluorescence of HA-Gly at pH 7.4, 8.0, and 9.0 (Fig. 1f). The fluorescence intensity is stable at pH 7.4 and 8.0, but decays single-exponentially at pH 9.0 (Fig. S1d), indicating conversion to a new species. Guided by chemical reasoning and LC-MS analysis (Figs. S9, 10), we assign this product to the ring-opened amic acid, HA-Gly_o (Fig. 1c). In contrast, HA-TAA showed essentially unchanged fluorescence intensity upon base addition (Fig. S20), consistent with the absence of the pH-responsive α-methyleneketone motif in its isoquinolinone structure. The results show that homophthalimides are more stable under basic conditions and exhibit reversible pH responses within a certain pH range, which forms the basis for the pH-dependent functionalities of elastomers discussed below.

Enabled by the carbonyl-rich ArKMK framework, homophthalimides (and HA-TAA) display long-lived delayed emission (Fig. 1g, i). The pristine crystal of HA-Gly (c-HA-Gly) exhibits only weak afterglow. We then melted c-HA-Gly and c-HA-Anl, and rapidly quenched them in liquid nitrogen to obtain the hypothesized "amorphous" solid, denoted a-HA-Gly and a-HA-Anl. Powder X-ray diffraction (PXRD) results indicate that a-HA-Gly contains a substantial amorphous fraction, whereas a-HA-Anl remains crystalline but as a polymorph (Fig. S21, 22). Comparative calculations further revealed stronger

https://doi.org/10.1038/s41467-026-79278-y

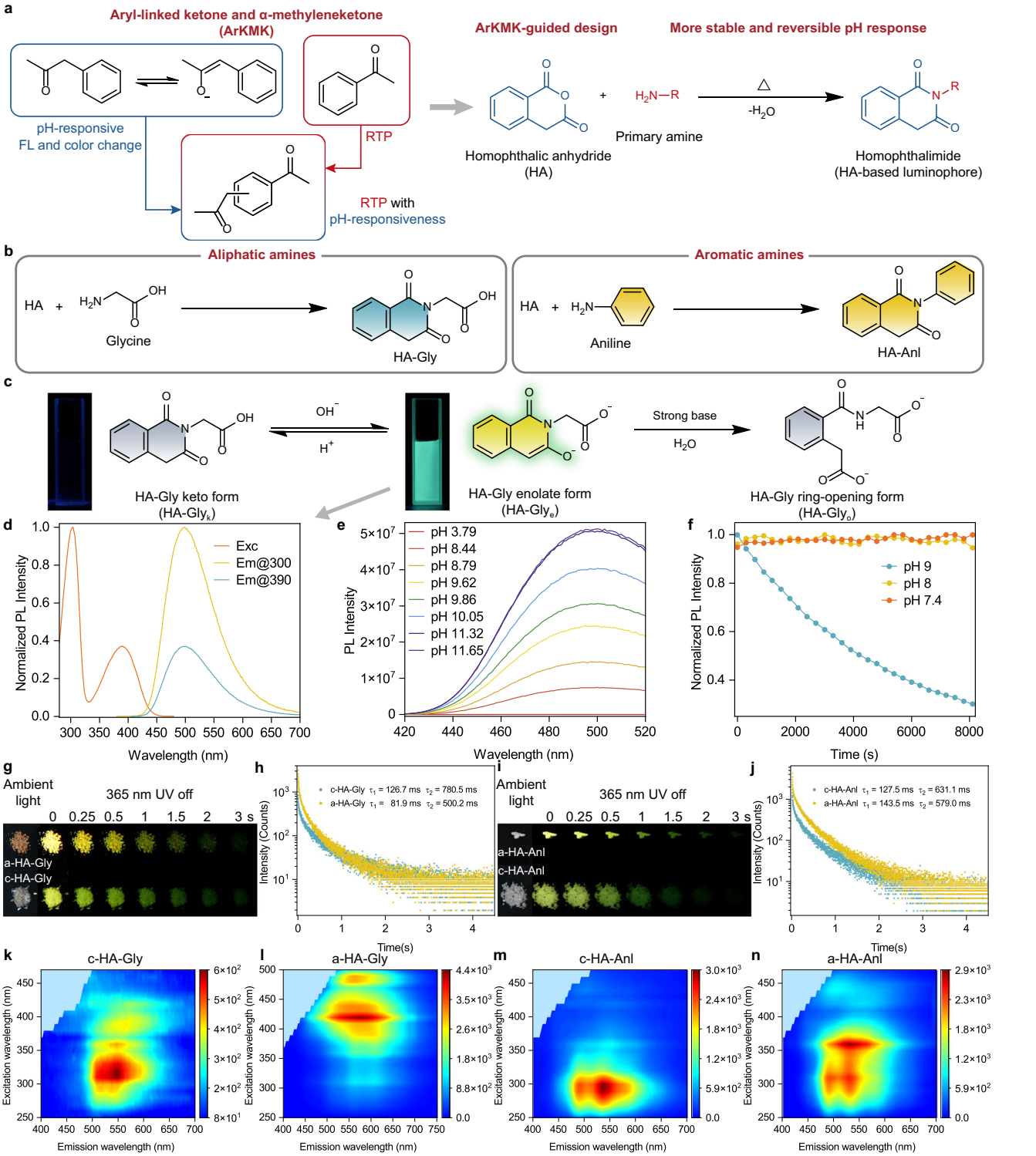

Fig. 1 | Synthesis, pH responsiveness and delayed emission of HA-based luminophores. a ArKMK design concept and general synthesis of HA-based luminophores from HA and primary amines. **b** Detailed scheme with representatives from aliphatic and aromatic amines. Thioacetamide pathway is a special case that gives methyl-isoquinolinone. **c** Schematic of the pH responsiveness of HA-Gly. **d** Excitation and emission spectra of HA-Gly under alkaline conditions. **e** Fluorescence emission spectra of HA-Gly at different pH. **f** Time course of fluorescence intensity of HA-Gly at different pH. **g**–**j** (**g**, **i**) Delayed emission photographs and (**h**, **j**) decay curves of HA-Gly and HA-Anl. **k**–**n** RTP excitation-emission-intensity contour maps of (**k**) c-HA-Gly, (**l**) a-HA-Gly, (**m**) c-HA-Anl and (**n**) a-HA-Anl.

dispersion and van der Waals contributions and more continuous aromatic-surface interactions in HA-Anl than in HA-Gly (Fig. S30). The larger π surface of HA-Anl may therefore facilitate cooperative molecular alignment and ordered packing during rapid cooling, likely contributing to its greater crystallization propensity. The RTP excitation-emission-intensity contour maps (hereafter, 3D maps) display a clear red shift of the dominant emission centers (Fig. 1k–n). To probe the origin of these differences, we performed single-crystal X-

ray diffraction (SCXRD) on c-HA-Gly and c-HA-Anl. c-HA-Gly adopts an anti-parallel arrangement in which the benzene and six-membered imide rings stack with counterparts in adjacent layers, while the glycine residue extends out of plane to form intermolecular H-bonds (Fig. S1e). In this packing, ring carbonyls remain well separated (minimum =O···O= distance ≈ 4.1 Å), yielding weak through-space conjugation and orbital interactions. In addition, extensive π-π stacking of the two-ring framework may provide nonradiative pathways that are detrimental to emission, limiting the overall photoluminescence efficiency. In a-HA-Gly, sharp cooling prevents relaxation to the most stable packing. The resulting scrambled arrangement disrupts part of the π-π stacking and increases the proximity and interactions among RTP favorable carbonyls. Long-wavelength emission centers therefore dominate (Fig. 1l vs 1k) and the quantum yield increases markedly (Table S2). c-HA-Anl exhibits a zig-zag packing pattern with moderately spaced carbonyls (minimum distance ≈ 3.4 Å) and offset aromatic contacts (Fig. S1f). Accordingly, its quantum yield exceeds that of c-HA-Gly, and the polymorphic a-HA-Anl retains a similar quantum yield while shifting toward longer-wavelength emission centers, likely aided by additional carbonyl interactions at grain boundaries (Fig. 1m vs n, Table S2). These observations show that molecular packing and phase order strongly govern both the spectra and efficiency of this luminophore family, and provide a handle for tuning RTP through crystallinity, polymorphism, and rapid-cooling-induced disorder.

Mechanistic study of long-lived emission in HA

Crystalline HA powder exhibits bright yellow-green afterglow upon 365 nm excitation (Fig. S2a) and, intriguingly, intrinsic band-shifting (excitation-wavelength-dependent shift)[31] in delayed emission: as the excitation wavelength increases, the emission peak redshifts and the afterglow color evolves from cyan-green to green, yellow, and ultimately orange (Fig. 2c, bottom). The delayed-emission 3D map shows two prominent emission centers (Fig. 2c). To trace their origin, we recorded 3D maps for HA at 77 K in dilute (10 μM) and concentrated (100 mM) THF solutions. Cryogenic temperatures constrain molecular motion and suppress nonradiative decay, yielding pronounced phosphorescence. In cryo-dilute solution, only one delayed-emission center appears at (290 (λ_{exc} max), 460 (λ_{em} max)) nm (Fig. 2a). In cryo-concentrated solution, the predominant center shifts to (310-330, 465) nm (Fig. 2b). These observations indicate that the two dominant emission centers in crystalline HA arise from monomer-like species (isolated-molecule emission center, IMEC) and collective species with substantial intermolecular interactions (collective emission center, CEC), respectively. The latter primarily redshifts the excitation band while leaving the T_1 energy only weakly perturbed. According to the SCXRD analysis of HA, the intermolecular interaction that dominates the RTP most likely arises from an =O···O (carbonyl and anhydride oxygen) contact with a distance of 2.86 Å (Fig. 2d). The UV-vis absorption of crystalline HA (Fig. 2e) shows a strong high-energy band with a weak red tail, separated by an inflection near 320 nm. This sudden falloff coincides with the boundary between IMEC and CEC in the RTP 3D map, indicating that IMEC is preferentially excited at λ_{exc} < 320 nm, whereas CEC dominates at λ_{exc} > 320 nm. Both contribute to the long-lived delayed emission. Multiple, excitation-dependent emission centers originating from a single luminophore are rarely reported, making the HA family a promising platform for multicolor applications.

Transient absorption spectroscopy (TAS) and temperature- and time-resolved photoluminescence measurements further resolve the underlying photophysical processes. Both femtosecond and nanosecond TAS reveal long-lived excited species, consistent with delayed emission originating from triplet states (Fig. 2g, h, and Supplementary Discussion). Temperature-dependent PL spectra of HA powder recorded from 77 K to 297 K under 280 to 400 nm excitation show an overall decrease in PL intensity upon heating. Notably, for longer-wavelength excitation (320-400 nm), an anomalous intensity reversal emerges between 107 and 137 K, where the steady-state PL increases with temperature. We ascribe this to an ultralong thermally activated delayed fluorescence (TADF)[32] contribution from the CEC with a relatively small singlet-triplet gap (ΔE_{ST}), which enables RISC ($T_1 \rightarrow S_1$) near 137 K and boosts steady-state emission. In contrast, 280 nm excitation predominantly addresses the IMEC with a larger ΔE_{ST}, hence the modest TADF cannot compensate for the usual thermal quenching and no intensity reversal is observed. Time-gated delayed emission spectra further resolve two emissive components (Fig. 2n–q). As the detection gate is shifted to later times, the blue emission band decays rapidly across all excitation wavelengths, whereas the long-wavelength profile remains nearly invariant, indicating a shorter-lived blue species and a longer-lived red-emitting species. The biexponential decay traces obtained from 290 and 355 nm excitation show features consistent with TADF and RTP (Fig. S2b, c).

DFT and TD-DFT calculations corroborate these observations. Relative to an isolated HA molecule, the periodic crystal exhibits a reduced HOMO-LUMO gap and a lower T_1 energy, consistent with the red-shifted excitation and phosphorescence bands in the condensed phase (Fig. 2r). The overarching photoluminescence picture of HA is summarized in Fig. 2s. In its isolated molecular form, HA features high-lying S_1 and T_1 energy levels and unconstrained intramolecular rotations and vibrations drive ultrafast nonradiative deactivation of both singlet and triplet excitons, leading to complete quenching of phosphorescence under ambient conditions. Upon crystallization, the rigid lattice effectively suppresses nonradiative pathways, while close intermolecular carbonyl-carbonyl contacts enable through-space electronic coupling, enhancing spin-orbit coupling and ISC to populate triplet states more effectively and giving rise to the two distinct emissive centers, IMEC and CEC. Moreover, CECs in the crystal further narrow the effective gap, producing a red-shifted excitation window and RTP emission (i.e., bandshifting), and partially enabling TADF via a reduced ΔE_{ST}. HA-Gly and HA-Anl display similar photophysical trends including biexponential decay kinetics analogous to those of their parent HA core, but their emission spectra and efficiencies vary with packing motifs and substituent-dependent electronic structures, indicating that microstructure and electronic configuration together govern their precise emissive behavior.

TPiO engineers controllable phase separation in polyester elastomers

To achieve well-defined phase separation in polyester elastomers, we developed a block-like segmentation strategy, denoted “two-pots-in-one” (TPiO), and implemented it in a citrate-based polymer system to introduce inter-segment mutual incompatibility that drives phase separation (Fig. 3a, Supplementary Discussion). Citrate-based polymers combine catalyst-free synthesis, excellent biocompatibility, and, importantly, intrinsic bioactivity for tissue regeneration arising from citrate-mediated metabolic modulation[33–35]. In practice, polyester backbone networks were obtained by polycondensation of citric acid and diols/polyols. We investigated the composition by varying the hydrophobic diol, synthesized the corresponding prepolymers, and confirmed that films derived from 1,10-decanediol and 1,12-dodecanediol exhibited clear phase separation and bright, persistent RTP, whereas shorter or cyclic diols were less effective (Fig. 3b, Supplementary Discussion). Considering biodegradability, the less hydrophobic 1,10-decanediol was selected for further study. To verify the necessity and effectiveness of the TPiO strategy in achieving well-defined, controllable phase separation and robust RTP in polyester elastomers, three synthesis methods were compared. In TPiO, hydrophilic and hydrophobic segments are partially preformed in separate flasks, which provides independent tunability akin to “blocks” in block copolymers, and are then mixed at a defined time point and further reacted to afford a phase-separated prepolymer (Fig. S3a). For

https://doi.org/10.1038/s41467-026-79278-y

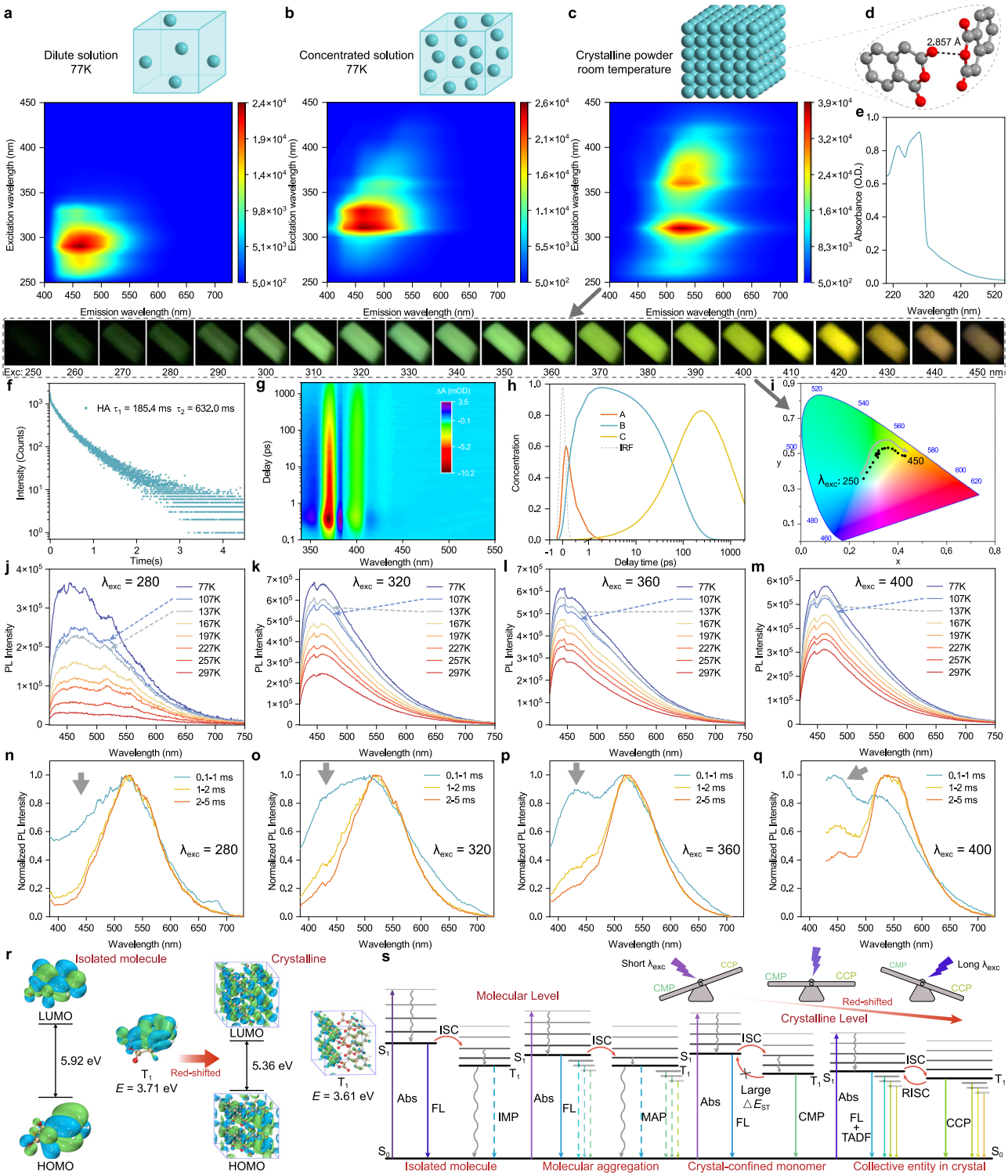

Fig. 2 | Photophysical properties and delayed-emission mechanisms of HA. a–c 3D maps of delayed emission for (**a**) dilute and (**b**) concentrated THF solutions at 77 K, and for (**c**) the crystal at room temperature (with photographs of excitation-wavelength-dependent emission colors shown below). **d** Representative crystal packing of HA showing intermolecular interactions and shortest O···O distances. **e** Absorption spectrum of HA crystalline powder. **f** Delayed-emission decay of HA crystalline powder monitored at 530 nm under 355 nm excitation. **g** Femtosecond transient absorption map of HA crystalline powder. **h** Excited-state kinetic components obtained from global analysis of the femtosecond transient absorption. **i** CIE 1931 chromaticity diagram of HA under various wavelengths. **j–m** Steady-state photoluminescence spectra of HA crystalline powder at different temperatures under excitation at (**j**) 280 nm, (**k**) 320 nm, (**l**) 360 nm, and (**m**) 400 nm. **n–q** Delayed-emission spectra of HA crystalline powder collected in different time windows under excitation at (**n**) 280 nm, (**o**) 320 nm, (**p**) 360 nm, and (**q**) 400 nm. **r**, DFT, and TD-DFT calculations for the isolated molecule and crystal of HA. **s** Jablonski diagram summarizing photophysical processes in different states of HA. IMP isolated-molecule phosphorescence, MAP molecular-aggregation phosphorescence, CMP crystal-confined-monomer phosphorescence, CCP crystal collective phosphorescence.

https://doi.org/10.1038/s41467-026-79278-y

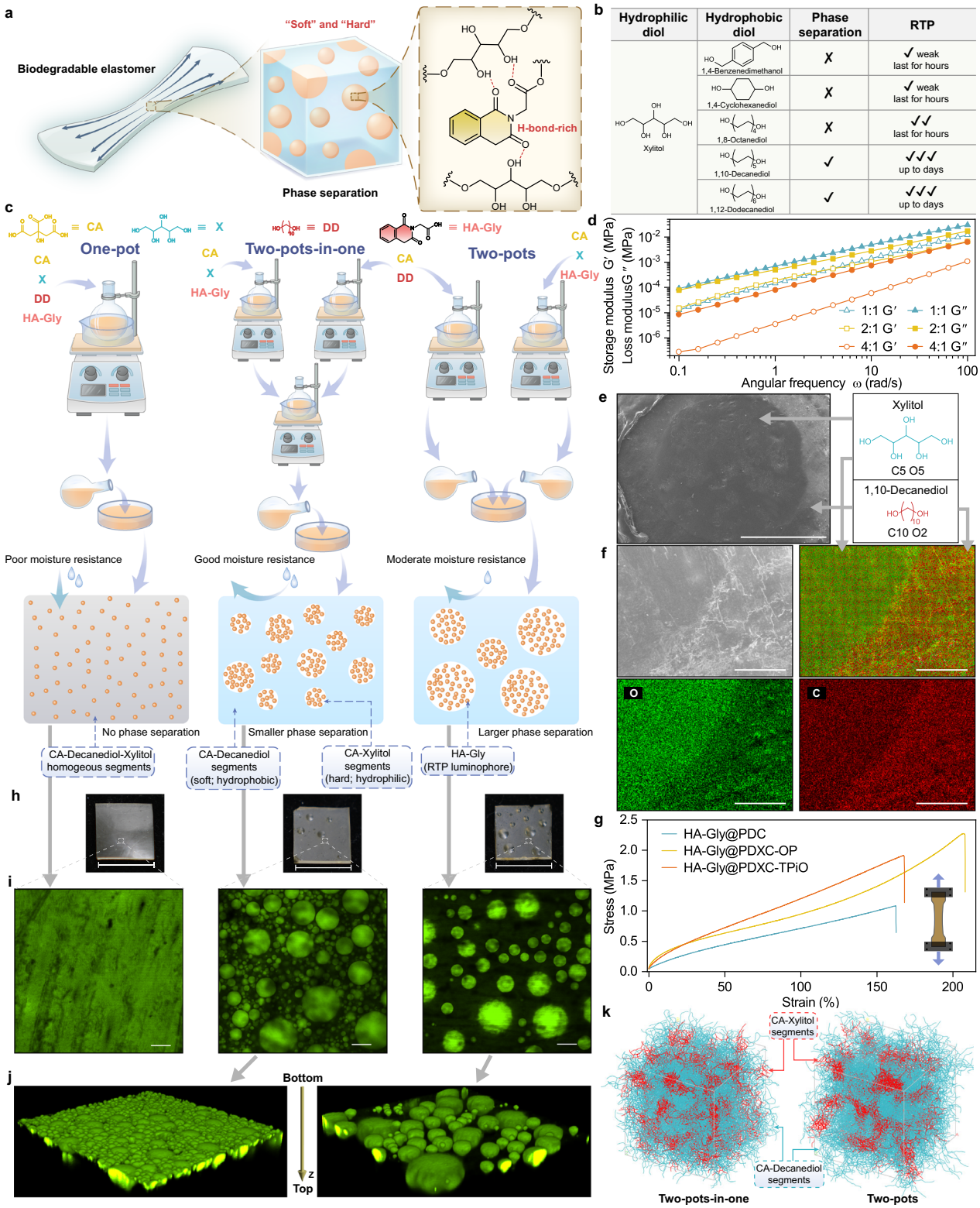

Fig. 3 | "Two-pots-in-one" synthesis of HA-citrate-based polyesters. a Rational design of HA-citrate-based, phase-separated elastomers. **b** Screening of polyesters prepared by the "two-pots-in-one" route using xylitol as the hydrophilic diol and the indicated hydrophobic diols. **c** Schematic comparison of "One-pot", "two-pots" and "two-pots-in-one" methods for synthesizing PDXC. **d** Frequency-dependent rheological behavior of PDXC prepolymers with different xylitol contents. **e** SEM image showing phase separation in a PDXC film. This experiment was repeated at least three times independently with similar results. Scale bar: 1 mm. **f** EDS maps of carbon and oxygen in a PDXC film. This experiment was repeated at least three times independently with similar results. Scale bar: 50 μm. **g** Comparison of uniaxial tensile properties of polymer films with different compositions or synthetic routes. **h**–**j** (**h**) Optical, scale bar: 1 cm; (**i**) confocal, scale bar: 20 μm; and (**j**) 3D reconstructed images of PDXC films produced by the "one-pot", "two-pots" and "two-pots-in-one" methods. This experiment was repeated at least three times independently with similar results. **k** Molecular dynamics simulations of phase separation for polymers obtained by the pure "two-pots" and "two-pots-in-one" methods.

example, in pot A, 0.01 mol of CA and xylitol were reacted for 30 min, followed by the addition of 0.001 mol of HA-Gly for another 30 min; in pot B, 0.02 mol of CA and an equimolar amount of 1,10-decanediol were reacted for 1 h. The two pots were mixed and allowed to react to completion (Fig. 3c), affording poly(1,10-decanediol-co-xylitol-co-citrate) (PDXC) with well-defined meso-to-macro phase separation. In contrast, the "one-pot" synthesis yields fully random incorporation of hydrophilic and hydrophobic monomers, effectively diluting the Flory-Huggins interaction parameter (χ) contrast and suppressing the thermodynamic driving force for phase separation, resulting in a homogeneous polymer. At the other extreme, a pure "two-pots" approach, which fully synthesizes each segment to completion and mixes them only during film casting, produces coarse, poorly controlled macrophase separation (Fig. 3h–j). Consequently, films prepared by TPiO display pronounced and long-lasting RTP, outperforming those from the other two routes, which we attribute to effective phase separation and improved moisture resistance (Supplementary Discussion).

Rheological data for PDXC prepolymers with decanediol-to-xylitol feed ratios of 4:1, 2:1, and 1:1 indicate a more sol-like than gel-like state and limited pre-networking, while increasing the xylitol fraction raises both G′ and G″, as well as viscosity, consistent with higher hydroxyl content and stronger H-bonding interactions (Fig. 3d, Fig. S3b). Considering the near-saturation of H-bonding interactions and suitable processability at the 2:1 composition, we selected this ratio for subsequent studies (Supplementary Discussion). Scanning electron microscopy (SEM) and energy-dispersive spectroscopy (EDS) mapping further reveal phase-separated microstructures, with xylitol- and luminophore-enriched domains appearing darker, consistent with higher electron density (Fig. 3e), and showing higher O content and correspondingly lower C content than the surrounding decanediol-rich (hydrophobic) matrix (Fig. 3f). Uniaxial tensile testing shows that incorporation of xylitol increases Young's modulus, tensile strength and fracture strain relative to HA-Gly@PDC (one-pot, citric acid + decanediol, no xylitol), and although phase separation (HA-Gly@PDXC-TPiO versus one-pot version, HA-Gly@PDXC-OP) slightly reduces the mechanical properties (Fig. 3g), the TPiO films retain higher mechanical performance than those prepared by the pure "two-pots" route (HA-Gly@PDXC-TP, Fig. S3c), possibly owing to interface effects. Molecular dynamics (MD) simulations further support that the pure "two-pots" method generates larger phase-separated domains (Fig. 3k).

Solvent-free processing refines phase separation and film performance

Further, reaction time can be exploited to tune phase separation (Fig. S4a–d). Shortening the pre-reaction from 1 h to 30 min suppresses the ultra-large domains and yields smaller, more numerous phase-separated droplets with rougher interfaces, as supported by confocal microscopy and MD simulations. However, two issues remain: (1) the domain sizes are still large (tens to hundreds of microns), and further decreasing the pre-reaction time does not shrink the domains (Supplementary Discussion); (2) the relatively large domain size and gradual solvent evaporation cause many domains to sediment toward the film bottom, producing z-axis inhomogeneity (Fig. 4a, 3j). To this end, we replaced dioxane-assisted processing with a solvent-free route, in which materials are processed directly in a heated, viscous liquid state. Confocal bright-field, fluorescence, and SEM images of solvent-free-processed films reveal much smaller domains with narrower size distributions (Fig. 4b–e). The through-thickness distribution is also homogeneous, as evidenced by the confocal 3D reconstruction (Fig. 4d). Ultra-small-angle X-ray scattering (USAXS) and 2D Fourier analysis of optical images[36] show a characteristic length scale consistent with nearly spherical droplet-like domains with average diameters of a few micrometers, confirming well-defined phase separation (Supplementary Discussion). Differential scanning calorimetry (DSC) shows well overlapped scans after a pre-cycle to erase thermal history, and two distinct T_gs (≈ −51 and 10 °C) are observed on cooling, whereas a single apparent T_g (≈ 11 °C) is seen on heating (Fig. S4e), which is characteristic of phase-separated polymer systems with such thermal hysteresis and scan-direction dependence[37,38]. Although the T_g of the hard domains is slightly below room temperature, variable-temperature FTIR revealed persistent and reversibly temperature-dependent hydrogen-bonding interactions well above T_g (Fig. S41), suggesting that hydrogen bonding, together with phase-separated organization and covalent network confinement, maintains a locally constrained environment for the luminophores. These results show that stable meso-to-micro-scale phase separation can be achieved by tailoring the synthetic and processing routes.

The HA-Gly@PDXC film exhibits bandshifting behavior arising from multiple emissive centers, accompanied by red-edge tails: afterglow images under 365 and 405 nm excitation are shown in Fig. 4j, and the 3D maps in Fig. 4k, Fig. S4f. This behavior differs markedly from HA-Gly in its molecular and crystalline states, highlighting the strong influence of molecular packing and the local microenvironment on emission. The structural origin of these multiple emissive features cannot be uniquely resolved from the present data. A plausible interpretation is that the heterogeneous polymer microenvironment generates an ensemble of local HA-Gly arrangements and interaction strengths, which in turn gives rise to a distribution of emissive-state energies. In terms of local order, polymer-bound HA-Gly is likely more similar to the disordered a-HA-Gly state than to the well-defined packing of c-HA-Gly, although its covalently confined polymer environment is distinct from either small-molecule state and this comparison should therefore be regarded as qualitative rather than a definitive structural assignment. Uniaxial tensile tests show that solvent-free processing leads to enhanced mechanical strength and stiffness, consistent with a denser polymer network and stronger intermolecular interactions compared to solvent-assisted processing (Fig. S4g). Consistently, delayed-emission images collected during stretching show no change in emission color (Fig. 4l). To further evaluate the effect of mechanical deformation on RTP, RTP 3D maps of the solvent-free HA-Gly@PDXC film were recorded before stretching, after one stretching-and-release cycle, and after ten cycles. The spectral profiles and peak positions remained essentially unchanged in all three states (Fig. S34). These results indicate that the emissive states responsible for RTP are preserved after mechanical deformation, supporting a mechanically robust interfacial microenvironment and stable photophysical behavior under applied strain. Considering the aqueous milieu of biomedical settings and the pH responsiveness of HA-Gly, we next examined the films' photophysical response in buffer. Upon immersion in pH 8.5 Tris-HCl buffer for 2 h, the steady-state PL intensity increased by more than 6-fold and the emission peak blue-shifted slightly (Fig. 4m, Fig. S4h), consistent with formation of the enolate form, HA-Gly_e. Intriguingly, water penetration can be directly visualized: hydrated regions become translucent while dry regions remain opaque (Fig. 4n bottom). Confocal imaging resolves three zones (Fig. 4n top, Fig. S4i): (1) a fully hydrated region that loses RTP, attributed to water competing for H-bonding with the matrix and disrupting luminophore confinement; (2) a penetration front where hydration is incomplete; and (3) an unhydrated region that retains RTP. In vitro degradation of film discs was evaluated under physiological buffer (pH 7.4 PBS, 37 °C). Although the continuous matrix is hydrophobic, water penetration is facilitated by the disintegration and leaching of dispersed hydrophilic domains, leading to progressive changes in the internal structure. The films exhibited progressive mass loss over 120 days, accompanied by eventual loss of macroscopic structural integrity at the late stage of degradation (Fig. S4j and Supplementary Discussion). Cytotoxicity assays show that HA-Gly is non-toxic even at millimolar concentrations (Fig. S43). The degradation profile matches soft-tissue repair

https://doi.org/10.1038/s41467-026-79278-y

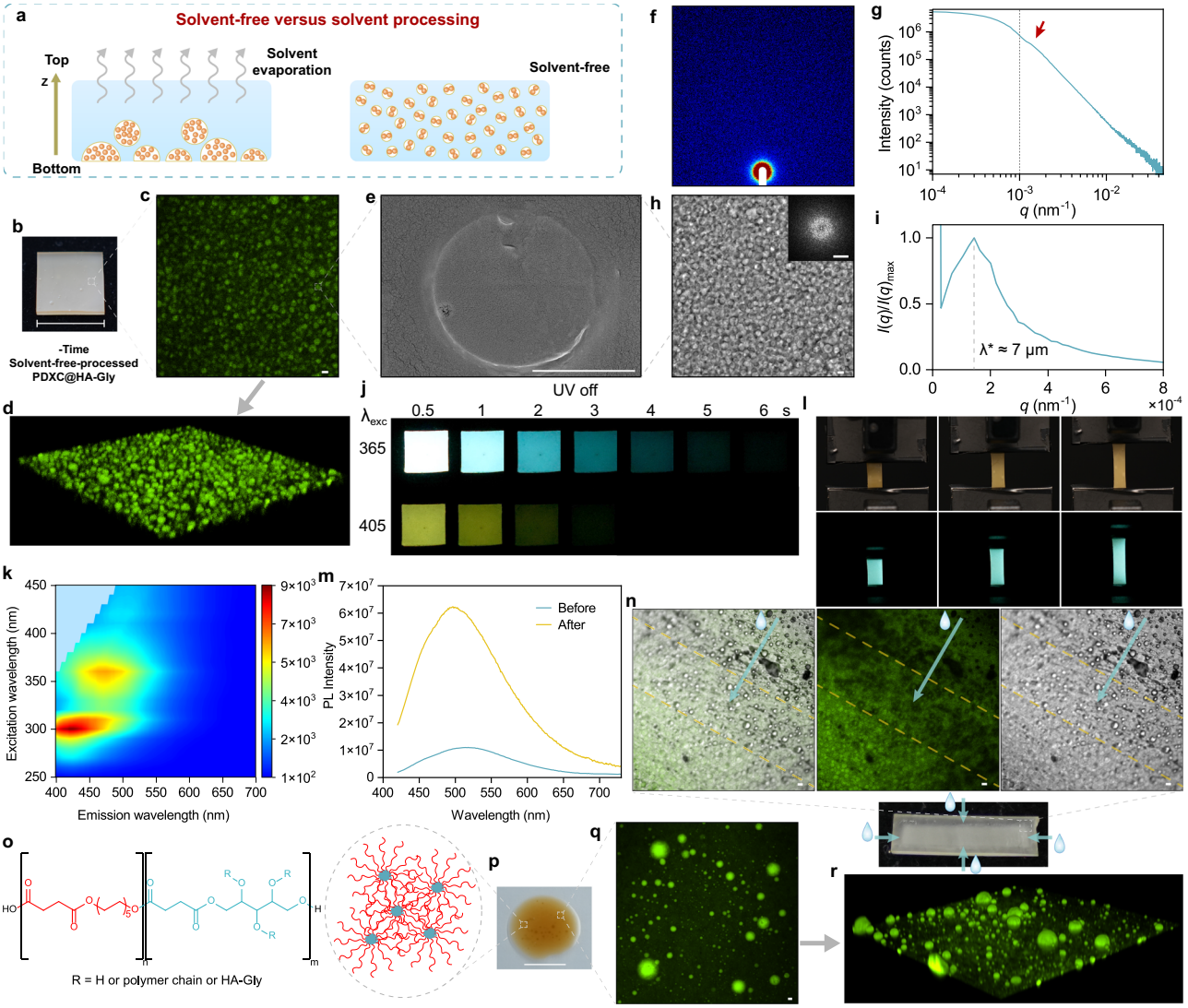

Fig. 4 | Further tuning and expansion of the "two-pots-in-one" method. **a** Schematic comparison of solvent and solvent-free film processing methods. **b**–**e** (**b**) Optical, scale bar: 1 cm; (**c**) confocal, scale bar: 5 μm; (**d**) 3D reconstructed and (**e**) SEM, scale bar: 2 μm; images of solvent-free HA-Gly@PDXC films. These experiments were repeated at least three times independently with similar results. **f, g** (**f**) USAXS 2D pattern and (**g**) corresponding I(q) vs q plot. **h, i** (**h**) Bright-field image of the solvent-free film with its 2D FFT (inset), scale bar: 5 μm, this experiment was repeated at least three times independently with similar results, and (**i**) Azimuthal average of 2D FFT of the microscopy image. **j** Photographs of afterglow from an HA-Gly@PDXC film after cessation of 365 and 405 nm excitation. **k** Delayed-emission 3D map of solvent-free HA-Gly@PDXC film. **l** Photographs of delayed emission of solvent-free HA-Gly@PDXC film during uniaxial stretch. **m** Fluorescence spectra of solvent-free HA-Gly@PDXC film before and after immersion in pH 8.5 Tris-HCl buffer for 2 h. Excitation wavelength: 405 nm. **n** Optical and confocal images of a partially water-penetrated solvent-free HA-Gly@PDXC film. This experiment was repeated at least three times independently with similar results. Scale bar: 5 μm. **o** Chemical structures and schematic illustration of a phase-separated succinate-based polymer, PDXS. **p**–**r** (**p**) Optical, scale bar: 1 cm; (**q**) confocal, scale bar: 10 μm; and (**r**) 3D reconstructed images of the phase-separated succinate-based polyester. This experiment was repeated at least three times independently with similar results.

timescales, with mechanical support retained over clinically relevant weeks[39–41]. In addition, rapid droplet-to-pore conversion generates persistent pathways for cell infiltration and neovascularization[42,43]. These results establish HA-Gly@PDXC as a mechanically robust, pH-responsive, and degradable polyester platform that couples stable RTP with tissue-relevant transport and remodeling behaviors.

To demonstrate generality, we applied TPiO to another polyester system composed of succinic acid (SA), 1,10-decanediol, and xylitol (Fig. 4o-r). Hydrophilic segments (SA, xylitol, and HA-Gly) and hydrophobic segments (SA and decanediol) were again preformed in separate pots (Fig. 4o). Because succinic acid is difunctional, the resulting polymer (PDXS) is more linear and thermoplastic with a much lower crosslinking density than citrate-based analogues (Fig. 4p) and exhibits spherical phase-separated domains with diameters ranging from a few to tens of micrometers (Fig. 4q, r). These domains persist through a melt-cool cycle, showing that the resulting phase separation is robust and the approach is valid beyond citrate-based elastomer systems (Supplementary Discussion).

Functional demonstrations of responsive phosphorescent elastomers

We next explored biomedical uses of HA-Gly@PDXC. First, subcutaneous implantation showed bright afterglow and enabled time-gated imaging (Fig. 5a), confirming feasibility for shallow implants. We then evaluated a more demanding scenario: tracking a swallowable caplet in the gastrointestinal (GI) tract (Fig. 5b and Supplementary Discussion). To directly assess intestinal imaging, we surgically placed a caplet molded from HA-Gly@PDXC in the ileum, returned

https://doi.org/10.1038/s41467-026-79278-y

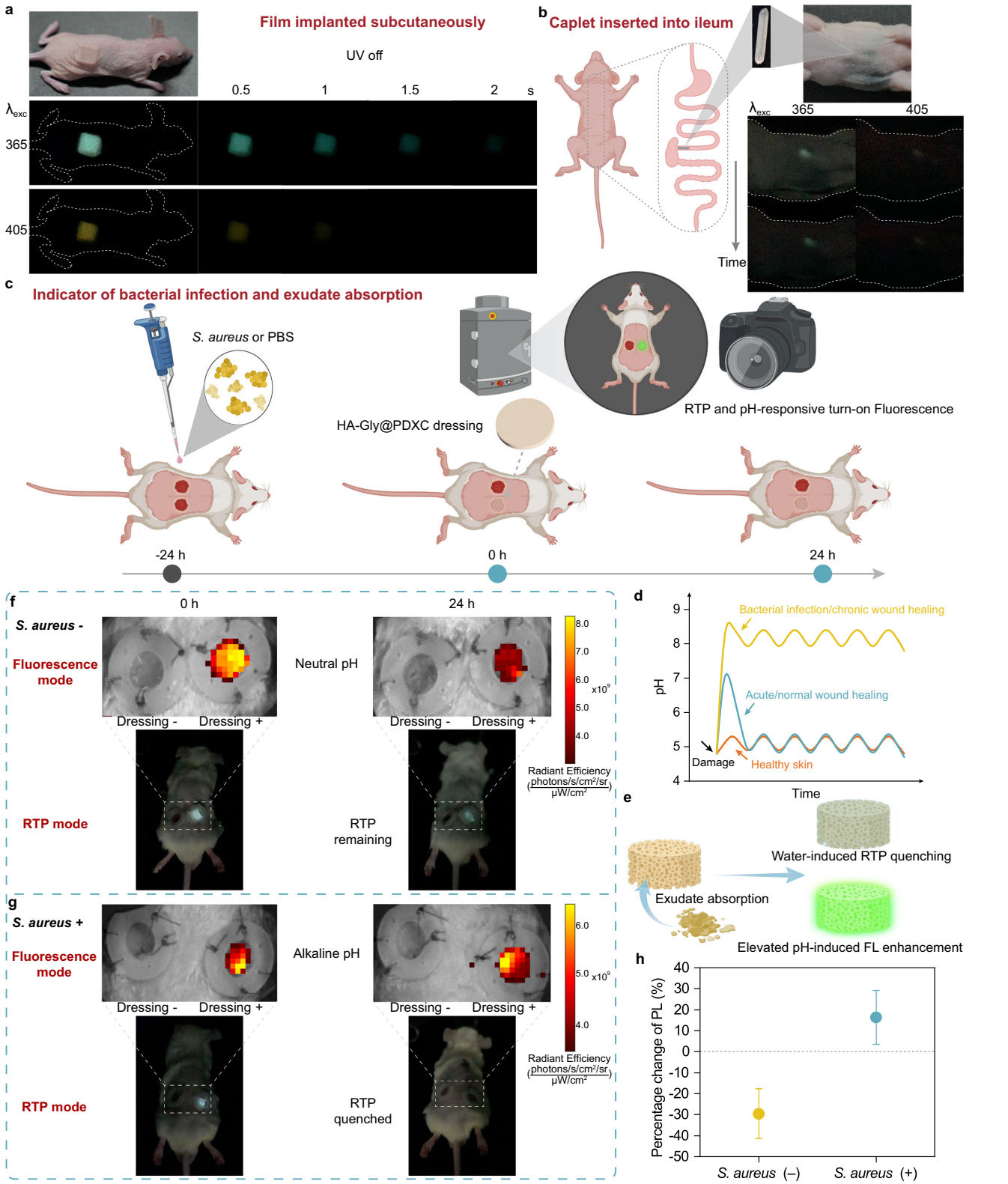

Fig. 5 | Biomedical application demonstrations of HA-Gly@PDXC. a Afterglow imaging of the subcutaneously implanted film. **b** Afterglow imaging of the caplet implanted into the small intestine (ileum). **c** Scheme of bacterial infection and exudate absorption indication in a mouse model. **d** Scheme of skin pH values under various physiological or pathological conditions. **e** Two luminescent modes for indicating bacterial infection and exudate absorption. Absorbed exudate quenches RTP and indicates that the dressing should be replaced, whereas alkaline exudate from an infected wound turns on pH-responsive fluorescence and increases the steady-state PL intensity. **f, g** In vivo imaging of skin wounds at 0 and 24 h with two luminescent modes. (**f**) Dressings on wounds without *S. aureus* inoculation showed decreased steady- state PL and remaining RTP after 24 h due to a limited volume of exudate; (**g**) Dressings on wounds with *S. aureus* inoculation showed increased steady-state PL and no RTP after 24 h due to a large volume of exudate. **h** Percentage change of steady-state PL intensity of the dressing with or without *S. aureus* infection. Data mean ± SD (n = 6, independent samples).

the bowel, and closed the abdominal wall. Under external 365 and 405 nm excitation at safety-compliant irradiance, delayed luminescence was recorded transabdominally. The long lifetime of RTP afforded a high signal-to-noise with effective autofluorescence rejection: 365 nm excitation produced a clear signal and 405 nm yielded a weaker yet discernible readout (Fig. 5b). Systemic biocompatibility was further confirmed by blood biochemistry and liver function analyses after caplet administration, which showed no significant differences compared with control animals. These results demonstrate the potential of HA-Gly@PDXC for in vivo imaging and monitoring in small animals.

Finally, we evaluated HA-Gly@PDXC as a smart wound dressing that integrates pH-responsive fluorescence with RTP. Normal skin exhibits an acidic pH, and during the physiological wound-healing process, skin pH increases to near-neutral levels upon exposure to interstitial fluid (pH 7.4), before returning to its native acidic state (Fig. 5d). However, pathological conditions such as bacterial infection and diabetes can elevate local wound pH to alkaline levels, thereby disrupting the normal wound healing cascade and leading to chronic wounds[11–13]. In parallel, chronic or infected wounds often generate abundant exudate, creating a clinical need for dressings that can indicate both wound chemistry and saturation state[44,45]. In this study, bacterial infection was selected as a representative pathological condition associated with an alkaline wound microenvironment. Our design leverages two orthogonal signals: exudate uptake progressively quenches RTP and extinguishes it upon saturation, indicating that replacement is needed, while alkaline exudate turns on pH-responsive fluorescence and increases steady-state PL intensity (Fig. 5e). In a mouse full-thickness skin-wound model (Fig. 5c), wounds inoculated with *S. aureus* showed complete RTP loss and increased fluorescence, whereas PBS-treated controls retained partial RTP and showed no fluorescence increase (Fig. 5f, g). Quantification across replicates confirmed a consistent fluorescence increase in infected wounds (about 30%) but a decrease in controls (about 17%) (Fig. 5h). Together, these results demonstrate dual-mode, noninvasive reporting of wound status using a single dressing platform.

Outlook

This study establishes a molecular-to-polymer strategy for coupling pH responsiveness with long-lived triplet emission in soft materials. At the molecular level, the ArKMK motif integrates proton-dependent keto-enolate chemistry with carbonyl-mediated intersystem crossing, allowing pH responsiveness and triplet-state photophysics to be programmed within the same luminophore framework. At the materials level, the TPiO strategy uses reaction sequence and segment incompatibility to generate phase-separated polyester networks, in which locally rigid microdomains stabilize triplet excitons while the surrounding matrix preserves bulk deformability. This design logic should be extendable by varying aromatic cores, carbonyl arrangements, substituents, and polymer architectures to tune triplet population, emission color, pKa, hydration response, degradation, and mechanical behavior. More generally, the combination of molecularly switchable luminescent states with reaction-sequence-controlled polymer microstructures offers a chemical strategy for designing soft photonic materials whose excited-state dynamics report local chemical and physical environments.

Methods

Materials

Homophthalic anhydride (97%), aniline (99%+), thioacetamide (99%), 1,10-decanediol (98%) and 1,12-dodecanediol (98%+) were purchased from Adamas. Glycine (99.5–100.5%) and xylitol (99%) were purchased from Macklin. All other chemicals and solvents were purchased from commercial suppliers and used as received unless otherwise stated. Detailed information on synthesis, purification, polymer preparation, and structural characterization is provided in the Supplementary Information.

Femtosecond transient absorption spectroscopy

Femtosecond transient absorption (fs-TA) measurements were carried out using a HARPIA-TA spectroscopy system (Light Conversion) combined with a frequency-doubled mode-locked Ti:sapphire femtosecond laser (Coherent) and an optical parametric amplifier (OPA). The amplified Ti:sapphire laser generated seed pulses with a pulse width of 35 fs at a repetition rate of 1 kHz. The seed pulses were split into two beams: one was directed into the OPA to generate a 360 nm pump pulse, while the other was focused onto a nonlinear crystal to produce a white-light continuum as a broadband UV-vis probe light. The excitation beam was kept at a low energy of 1 μJ /cm^2 per pulse to avoid the exciton-exciton and exciton-charge annihilation effects. The time delay between the pump and probe pulses was adjusted by a mechanical delay stage. All measurements were performed at room temperature.

Nanosecond transient absorption spectroscopy

Nanosecond transient absorption (ns-TA) measurements were conducted using a customized diffuse reflectance setup. Samples were excited at 355 nm, and a pulsed xenon flash lamp with an energy of ~100 μJ per pulse was used as the probe light source. Transient absorption signals were detected using a gated ICCD camera (Andor iStar). The system's performance and reliability were validated using benzophenone powder as a reference. All measurements were conducted at room temperature.

Rheological tests

Strain sweeps (0.1%-100%, 1 Hz) were performed first to determine the linear viscoelastic region. Frequency sweeps were then carried out at a fixed strain of 1%. All measurements were performed at room temperature.

Uniaxial tensile tests

Polymer film specimens were cut into dog-bone shapes with a gauge length of 10 mm and a width of 2 mm. The thickness of the gauge region (~1 mm) was measured individually for each specimen prior to testing. Tensile tests were conducted at a constant strain rate corresponding to a crosshead speed of 60 mm/min. Young's modulus ($E = \sigma/\varepsilon$) was calculated from the initial linear region of the stress-strain curve (1–3% tensile strain). All tensile tests were conducted on dry films at room temperature under ambient conditions.

Delayed-emission imaging and spectral characterization under tensile deformation

Delayed-emission videos under tensile strain were recorded during uniaxial stretching using a universal tensile testing machine. Rectangular films (1 × 3 cm, thickness ~1 mm) were stretched at 5 mm/min. During stretching, the samples were periodically excited with a 365 nm UV flash LED to trigger delayed-emission throughout the stretching process until fracture occurred.

To evaluate the stability of the RTP characteristics after repeated mechanical deformation, separate film specimens were repeatedly stretched to 50% strain and subsequently released to the original gauge length at a crosshead speed of 5 mm/min. RTP excitation-emission 3D maps were recorded for the same film before stretching, after one stretching-and-release cycle, and after ten stretching-and-release cycles. The film was measured in the fully released state after each designated number of cycles, and identical spectroscopic settings were used for all measurements.

Fourier-transform infrared spectroscopy
For variable-temperature FTIR measurements, the polymer film was mounted in a temperature-controlled transmission accessory equipped with CaF_2 windows. Spectra were collected sequentially at 27, 40, 60, and 80 °C during heating. The sample was subsequently cooled back to 27 °C, and an additional spectrum was collected to evaluate the reversibility of the temperature-dependent spectral changes.

Equilibrium swelling and sol-fraction measurements
Polymer films were thermally crosslinked at 80 °C for 3 days and then punched into circular discs with a diameter of 6 mm. The initial dry mass of each disc (M_i) was recorded before immersion in DMSO. The discs were immersed in DMSO at room temperature for 72 h to reach equilibrium swelling. After swelling, the discs were removed from the medium, and excess DMSO on the surface was gently blotted with filter paper before the swollen mass (M_w) was measured. The swollen discs were then freeze-dried for 48 h and weighed again to obtain the final dry mass (M_d).

Differential scanning calorimetry measurements
The DSC measurements of the films were performed at a heating and cooling rate of 10 °C/min from −80 to 200 °C under a nitrogen atmosphere with a purge flow rate of 50 mL/min. The samples were subjected to three consecutive heating-cooling cycles. The first heating run, starting from room temperature, was used to erase the thermal history of the sample, and the subsequent two heating-cooling cycles were used for analysis.

In vitro degradation study
Polymer films were cut into round disks (6 mm diameter, thickness ~1 mm) and immersed in 10 mL of PBS (pH 7.4). Samples were incubated at 37 °C, with PBS refreshed weekly. At predetermined time points, the disks were taken out, lyophilized, and weighed. The degradation was assessed by calculating mass loss according to:

$$\text{Mass loss}(\%) = (M_0 - M_n)/M_0 \times 100$$

where M_0 is the initial dry mass and M_n is the dry mass after incubation.

Cytotoxicity assessments
BALB/3T3 clone A31 fibroblast cells were purchased from HyCyte (#TCM-C714, Suzhou, China) and were cultured in high-glucose Dulbecco's Modified Eagle Medium (DMEM, Gibco) containing 10% fetal bovine serum (FBS, Gibco) at 37 °C in a humidified incubator with 5% CO_2. The cells were seeded in a 96-well plate at a density of 3000 cells per well. The cells were incubated overnight to ensure cell attachment. Different concentrations of HA-Gly in DMEM were added to the cells, which were then incubated for 24 h. Cell viability was determined using both the Cell Counting Kit-8 (CCK-8, Lablead) assay and the CellTiter-Lumi Plus Luminescent Cell Viability Assay Kit following the manufacturer's instructions. The absorbance and bioluminescence were measured using a microplate reader.

Afterglow imaging
Afterglow imaging was performed using a digital camera (Sony α7 II; ISO 64,000; aperture f/2.8). Excitation was provided by 365 and 405 nm flash LEDs. The excitation conditions were selected to comply with maximum permissible exposure limits based on combined photochemical (ICNIRP, 2004) and thermal (IEC 6247) safety thresholds, corresponding to a power density of 200 mW/cm^2 for up to 10 s. Power density was measured using a Thorlabs PM100D power meter equipped with an S130VC silicon detector.

Animals
All animal experiments were conducted in accordance with protocols approved by the Institutional Animal Care and Use Committee (IACUC) of Westlake University (protocol number AP#25-149-YJ). The animals were housed under controlled environmental conditions with a 12 h light/dark cycle, ambient temperature of 22–24 °C, and relative humidity of 40–60%. Five-week-old BALB/c-nude mice were used for subcutaneous implant imaging and afterglow GI imaging, while eight-week-old BALB/c mice were used for wound dressing experiments.

Subcutaneous implant imaging
Nude mice were anesthetized by intraperitoneal injection of pentobarbital sodium (60 mg/kg body weight), and HA-Gly@PDXC films (10 × 10 × 0.5 mm) were implanted subcutaneously on the dorsal side through a small incision. The incision was closed using absorbable sutures. Immediately after surgery, the implant site was imaged.

Afterglow GI imaging
Caplets made of solvent-free HA-Gly@PDXC were administered esophageally to nude mice using a syringe feeder. After administration, delayed-emission imaging was attempted under isoflurane anesthesia, following excitation at 365 nm. At predefined time points (15 min or 2 h post-administration), mice were euthanized for anatomical inspection. For direct intestinal imaging, a caplet was surgically placed into the distal ileum (near the cecum) of a euthanized mouse. The bowel was repositioned to its original location, and the abdominal wall was closed, followed by imaging (exposure time 1/3 s).

Blood routine and liver function assessments
At 24 h after esophageal administration of the caplet, blood samples were collected from nude mice for biochemical analysis using a Hitachi Automatic Analyzer 3110. Parameters analyzed included aspartate aminotransferase (AST), alanine aminotransferase (ALT), ALT/AST ratio, albumin (ALB), total protein (TP), globulin (GLB), alkaline phosphatase (ALP), total cholesterol (CHO), creatinine (CREA), γ-glutamyl transferase (GGT), glucose (GLU), total bilirubin (TBIL), triglycerides (TG), urea (UREA), and electrolytes (Ca, P, K, Na, and Cl).

Wound dressing
The BALB/c mice were anesthetized with isoflurane, and the dorsal hair was shaved and disinfected. Two full-thickness wounds (6 mm in diameter) were created on the dorsum using surgical scissors. To minimize wound contraction, silicone splint rings were placed around the wounds and fixed with 5-0 absorbable sutures. Mice were randomly divided into two groups (n = 6): (1) Infection group, in which wounds were inoculated with 10 μL of S. aureus suspension (1×10^9 CFU/mL; total dose 1×10^7 CFU); (2) Control group, in which wounds received 10 μL of sterile PBS (pH 7.4). After 24 h, the wounds were inspected to confirm the successful establishment of the infection model. For each mouse, one wound was fully covered with an HA-Gly@PDXC film, while the other was left uncovered as a control. Imaging was performed immediately after dressing application. Both wounds were then sealed with a transparent film dressing (Tegaderm, 3 M). A second round of imaging was conducted 24 h later. Fluorescence imaging was performed using an IVIS Lumina III In Vivo Imaging System operated in fluorescence mode (excitation filter: 420 nm; emission filter: 520 nm) to monitor turn-on fluorescence. Phosphorescence videos of the HA-Gly@PDXC wound dressings under pulsed UV excitation (365 nm) were recorded using a camera (exposure time 1/100 s).

Reporting summary
Further information on research design is available in the Nature Portfolio Reporting Summary linked to this article.

Data availability

The data supporting the findings of this study are available within the Article and its Supplementary Information, or available from the corresponding authors on request. Crystallographic data for HA-Gly, HA-Anl, and HA-TAA are available from the Cambridge Crystallographic Data Center under reference numbers CCDC 2525488, 2525489, and 2525487, respectively. Source data are provided with this paper.

Code availability

Custom scripts used for 2D FFT analysis are available from the corresponding author upon request.

References

1. An, Z. et al. Stabilizing triplet excited states for ultralong organic phosphorescence. *Nat. Mater.* **14**, 685–690 (2015).
2. Zhao, W., He, Z. & Tang, B. Z. Room-temperature phosphorescence from organic aggregates. *Nat. Rev. Mater.* **5**, 869–885 (2020).
3. Yang, J. et al. The influence of the molecular packing on the room temperature phosphorescence of purely organic luminogens. *Nat. Commun.* **9**, 840 (2018).
4. Zhang, L. et al. White light-excited organic room-temperature phosphorescence for improved in vivo bioimaging. *Nat. Commun.* **16**, 3970 (2025).
5. Zhao, M. et al. Electrical signals control wound healing through phosphatidylinositol-3-OH kinase-γ and PTEN. *Nature* **442**, 457–460 (2006).
6. Kalidasan, V. et al. Wirelessly operated bioelectronic sutures for the monitoring of deep surgical wounds. *Nat. Biomed. Eng.* **5**, 1217–1227 (2021).
7. Gao, Y. et al. A flexible multiplexed immunosensor for point-of-care in situ wound monitoring. *Sci. Adv.* **7**, eabg9614 (2021).
8. Marks, H. et al. A paintable phosphorescent bandage for post-operative tissue oxygen assessment in DIEP flap reconstruction. *Sci. Adv.* **6**, eabd1061 (2020).
9. Jiang, Y. et al. Wireless, closed-loop, smart bandage with integrated sensors and stimulators for advanced wound care and accelerated healing. *Nat. Biotechnol.* **41**, 652–662 (2023).
10. Cox, T. R. & Erler, J. T. Remodeling and homeostasis of the extracellular matrix: implications for fibrotic diseases and cancer. *Dis. Model. Mech.* **4**, 165–178 (2011).
11. Schneider, L. A., Korber, A., Grabbe, S. & Dissemond, J. Influence of pH on wound-healing: a new perspective for wound-therapy? *Arch. Dermatological Res.* **298**, 413–420 (2007).
12. Percival, S. L., McCarty, S., Hunt, J. A. & Woods, E. J. The effects of pH on wound healing, biofilms, and antimicrobial efficacy. *Wound Repair Regeneration* **22**, 174–186 (2014).
13. Jones, E. M., Cochrane, C. A. & Percival, S. L. The effect of ph on the extracellular matrix and biofilms. *Adv. Wound Care* **4**, 431–439 (2015).
14. Bolton, O., Lee, K., Kim, H.-J., Lin, K. Y. & Kim, J. Activating efficient phosphorescence from purely organic materials by crystal design. *Nat. Chem.* **3**, 205–210 (2011).
15. Gu, L. et al. Colour-tunable ultra-long organic phosphorescence of a single-component molecular crystal. *Nat. Photonics* **13**, 406–411 (2019).
16. Li, Q. et al. Induction of long-lived room temperature phosphorescence of carbon dots by water in hydrogen-bonded matrices. *Nat. Commun.* **9**, 734 (2018).
17. Kenry, Chen, C. & Liu, B. Enhancing the performance of pure organic room-temperature phosphorescent luminophores. *Nat. Commun.* **10**, 2111 (2019).
18. Yang, Z. et al. Intermolecular electronic coupling of organic units for efficient persistent room-temperature phosphorescence. *Angew. Chem. Int. Ed.* **55**, 2181–2185 (2016).
19. Wang, D., Wang, Y., Zimudzi, T. J., Chen, L.-Q. & Yang, J. Harnessing the duality of bases toward controlled color and fluorescence. *Sci. Adv.* **10**, eadn9692 (2024).
20. Gan, N. et al. Stretchable phosphorescent polymers by multiphase engineering. *Nat. Commun.* **15**, 4113 (2024).
21. Chen, M. et al. Stretchable, ultralong room-temperature phosphorescence poly(urethane-urea) elastomer resistant to humidity and heat. *Adv. Mater.* **37**, 2504825 (2025).
22. Ye, H., Zhang, K., Kai, D., Li, Z. & Loh, X. J. Polyester elastomers for soft tissue engineering. *Chem. Soc. Rev.* **47**, 4545–4580 (2018).
23. Wang, Y., Ameer, G. A., Sheppard, B. J. & Langer, R. A tough biodegradable elastomer. *Nat. Biotechnol.* **20**, 602–606 (2002).
24. Yang, J., Webb, A. R. & Ameer, G. A. Novel citric acid-based biodegradable elastomers for tissue engineering. *Adv. Mater.* **16**, 511–516 (2004).
25. Moreau, M. F., Chappard, D., Lesourd, M., Monthéard, J. P. & Baslé, M. F. Free radicals and side products released during methylmethacrylate polymerization are cytotoxic for osteoblastic cells. *J. Biomed. Mater. Res.* **40**, 124–131 (1998).
26. Wendels, S. & Avérous, L. Biobased polyurethanes for biomedical applications. *Bioact. Mater.* **6**, 1083–1106 (2021).
27. Tanzi, M. C. et al. Cytotoxicity of some catalysts commonly used in the synthesis of copolymers for biomedical use. *J. Mater. Sci.: Mater. Med.* **5**, 393–396 (1994).
28. Malamas, M. S. & Hohman, T. C. N-Substituted spirosuccinimide, spiropyridazine, spiroazetidine, and acetic acid aldose reductase inhibitors derived from isoquinoline-1,3-diones. 2. *J. Med. Chem.* **37**, 2059–2070 (1994).
29. Yuan, Y.-C. et al. Unmasking amides: ruthenium-catalyzed protodecarbonylation of n-substituted phthalimide derivatives. *Org. Lett.* **19**, 6404–6407 (2017).
30. Sakamoto, T., An-Naka, M., Kondo, Y. & Yamanaka, H. Condensed heteroaromatic ring systems. VIII.: Synthesis of 3-substituted isocoumarins from o-halobenzoic acid derivatives. *Chem. Pharm. Bull. (Tokyo)* **34**, 2754–2759 (1986).
31. Wang, D. et al. Citric acid-based intrinsic band-shifting photoluminescent materials. *Research* **6**, 0152 (2023).
32. Xiao, Y., Shen, M., Chan, C.-Y., Yu, T. & Huang, W. Ultralong organic afterglow from small molecular host-guest materials: state of the art. *Light.: Sci. Appl.* **14**, 290 (2025).
33. Ma, C. et al. Citrate-based materials fuel human stem cells by metabonegenic regulation. *Proc. Natl. Acad. Sci. USA* **115**, E11741–E11750 (2018).
34. Xu, H. et al. Citric acid: A nexus between cellular mechanisms and biomaterial innovations. *Adv. Mater.* **36**, 2402871 (2024).
35. Xu, H. et al. Metabotissugenic citrate biomaterials orchestrate bone regeneration via citrate-mediated signaling pathways. *Sci. Adv.* **11**, eady2862 (2025).
36. Fernández-Rico, C. et al. Elastic microphase separation produces robust bicontinuous materials. *Nat. Mater.* **23**, 124–130 (2024).
37. Bizmark, N. et al. Hysteresis in the thermally induced phase transition of cellulose ethers. *Soft Matter* **18**, 6254–6263 (2022).
38. Wunderlich, B. *Thermal analysis of polymeric materials*. (Springer, 2005).
39. Boateng, J. S., Matthews, K. H., Stevens, H. N. E. & Eccleston, G. M. Wound healing dressings and drug delivery systems: a review. *J. Pharm. Sci.* **97**, 2892–2923 (2008).
40. Guo, S. & DiPietro, L. A. Factors affecting wound healing. *J. Dent. Res.* **89**, 219–229 (2010).
41. Rodrigues, M., Kosaric, N., Bonham, C. A. & Gurtner, G. C. Wound healing: A cellular perspective. *Physiological Rev.* **99**, 665–706 (2019).
42. Murphy, C. M., Haugh, M. G. & O'Brien, F. J. The effect of mean pore size on cell attachment, proliferation and migration in

collagen–glycosaminoglycan scaffolds for bone tissue engineering. *Biomaterials* **31**, 461–466 (2010).
43. Xia, P. & Luo, Y. Vascularization in tissue engineering: The architecture cues of pores in scaffolds. *J. Biomed. Mater. Res. Part B: Appl. Biomater.* **110**, 1206–1214 (2022).
44. Cutting, K. F. & White, R. J. Avoidance and management of periwound maceration of the skin. *Professional Nurse (Lond., Engl.)* **18**, 35–36 (2002). 33.
45. Schultz, G. S. et al. Wound bed preparation: a systematic approach to wound management. *Wound Repair Regen.* **11**, S1–S28 (2003).

Acknowledgements

We thank M. Chen from Westlake University for help on rheology measurements, Z. Zheng from Westlake University for help on DSC measurements, Z. Gao from Westlake University for help on caplet mold design, W. Cao from Instrumentation and Service Center for Physical Sciences at Westlake University for the assistance in SEM and EDS characterizations, Z. Chen from Instrumentation and Service Center for Molecular Sciences at Westlake University for the assistance in some temperature-dependent PL measurements, X. Miao from Instrumentation and Service Center for Physical Sciences at Westlake University for help on single-crystal X-ray diffraction analysis, Anton Paar Inc. for help on USAXS measurements and analysis, Unisoku Co., Ltd. for help on ns-TA measurements and analysis. Figure 5b, c, e were partially created using BioRender. Wang, D. (2026) https://BioRender.com/luufs6y.

Author contributions

D.W. conceived the project, performed most of the experiments, analyzed the data, gave suggestions on the DFT calculations and prepared the draft of the manuscript; J.F. performed DFT calculations and cell cytotoxicity experiments, assisted with some experiments; and J.Y. supervised the project. All authors revised and contributed to the final version of the manuscript.

Funding

D. W. acknowledges the support from the National Natural Science Foundation of China (32501225). J. Y. acknowledges the support from the National Key Research and Development Program of China (2024YFA1107800).

Competing interests

The authors declare no competing interests.

Additional information

Supplementary information The online version contains supplementary material available at https://doi.org/10.1038/s41467-026-79278-y.

Correspondence and requests for materials should be addressed to Jian Yang.

Peer review information *Nature Communications* thanks Bo Lei and the other anonymous reviewer(s) for their contribution to the peer review of this work. A peer review file is available.

Reprints and permissions information is available at http://www.nature.com/reprints

Publisher's note Springer Nature remains neutral with regard to jurisdictional claims in published maps and institutional affiliations.

Open Access This article is licensed under a Creative Commons Attribution-NonCommercial-NoDerivatives 4.0 International License, which permits any non-commercial use, sharing, distribution and reproduction in any medium or format, as long as you give appropriate credit to the original author(s) and the source, provide a link to the Creative Commons licence, and indicate if you modified the licensed material. You do not have permission under this licence to share adapted material derived from this article or parts of it. The images or other third party material in this article are included in the article's Creative Commons licence, unless indicated otherwise in a credit line to the material. If material is not included in the article's Creative Commons licence and your intended use is not permitted by statutory regulation or exceeds the permitted use, you will need to obtain permission directly from the copyright holder. To view a copy of this licence, visit http://creativecommons.org/licenses/by-nc-nd/4.0/.

© The Author(s) 2026

This Article in Press is shared early to give you faster access to new research. It is citable and carries a permanent DOI. The final edited version will replace it automatically.